PHILOSOPHICAL TRANSACTIONS A

rsta.royalsocietypublishing.org

Research

Article submitted to journal

Subject Areas:
xxxxx, xxxxx, xxxx

Keywords:
geophysical fluid dynamics, potential vorticity (PV) inversion, singular limit, rapid rotation, strong stratification

Author for correspondence:
Yeyu Zhang
e-mail:
zhangyeyu@mail.shufe.edu.cn

Submitted on August 3, 2021
Revised on December 15, 2021

Convergence to precipitating quasi-geostrophic equations with phase changes: Asymptotics and numerical assessment

Yeyu Zhang[1], Leslie M. Smith[2,3] and Samuel N. Stechmann[2,4]

[1]School of Mathematics, Shanghai University of Finance and Economics, Shanghai 200433, PR China
[2]Department of Mathematics, University of Wisconsin-Madison, Madison, Wisconsin 53706, USA
[3]Department of Engineering Physics, University of Wisconsin-Madison, Madison, Wisconsin 53706, USA
[4]Department of Atmospheric and Oceanic Sciences, University of Wisconsin-Madison, Madison, Wisconsin 53706, USA

The quasi-geostrophic (QG) equations play a crucial role in our understanding of atmospheric and oceanic fluid dynamics. Nevertheless, the traditional QG equations describe "dry" dynamics that do not account for moisture and clouds. To move beyond the dry setting, precipitating QG (PQG) equations have been derived recently using formal asymptotics. Here, we investigate whether the moist Boussinesq equations with phase changes will converge to the PQG equations. A priori, it is possible that the nonlinearity at the phase interface (cloud edge) may complicate convergence. A numerical investigation of convergence or non-convergence is presented here. The numerical simulations consider cases of $\epsilon = 0.1$, 0.01, and 0.001, where ϵ is proportional to the Rossby and Froude numbers. In the numerical simulations, the magnitude of vertical velocity w (or other measures of imbalance and inertio-gravity waves) is seen to be approximately proportional to ϵ as ϵ decreases, which suggests convergence to PQG dynamics. These measures are quantified at a fixed time T that is $O(1)$, and the numerical data also suggests the possibility of convergence at later times.

THE ROYAL SOCIETY PUBLISHING

1. Introduction

The quasi-geostrophic (QG) equations are one of the fundamental systems of atmospheric and oceanic fluid dynamics. They provide a simplified setting for understanding a variety of phenomena, such as baroclinic instability [1–3] and geostrophic turbulence [4–6].

The QG approximation is an asymptotic limit, and it applies to fluids that are rapidly rotating and strongly stratified, as quantified by small Rossby and Froude numbers, respectively. Mathematically, in this limit, solutions to the Boussinesq equations can be rigorously proved to converge to solutions of the QG equations [7,8].

Despite their fundamental role, the traditional QG equations are a "dry" system in the sense that they do not account for moisture, clouds, and precipitation. When phase changes of water are present, the evolution of the potential temperature in the Boussinesq equations is modified to be

$$\frac{D\theta}{Dt} = \frac{L_v}{c_p} C, \tag{1.1}$$

where C represents condensation and evaporation, c_p is the specific heat capacity, and L_v is the latent heat of vaporization [9,10]. Additional equations are also needed for water quantities such as the water vapor mixing ratio q_v and other variables that measure the liquid water content.

In this moist case, several proposals had been made to supplement the dry QG equations with a moisture variable and/or latent heating [11–16], and these studies have provided valuable insight into the effects of moisture and latent heating. Nevertheless, these proposals treated moisture somewhat as a supplement or add-on to the dry QG system, which complicates the formulation of a precise connection between these moist QG systems and the moist Boussinesq equations.

In recent work [17], a moist QG limit has been proposed for the moist system as a whole, and the limiting system was called the precipitating QG (PQG) equations. The PQG limit is a moist analog of the dry QG limit of small Rossby and Froude numbers, and, as such, it is possible to consider the convergence of the moist Boussinesq equations to the PQG equations in this limit. While this limit has been formulated via formal asymptotics [17], no rigorous proof of convergence has yet been shown.

Here, a numerical investigation of convergence or non-convergence is conducted. While rigorous convergence has been proved for the dry QG limit, there are several reasons why the PQG limit may be non-converging. One reason for possible non-convergence is the complication of phase changes, which introduce nonlinear thresholds as in condensation/evaporation C in (1.1). Phase changes and latent heating may provide new mechanisms for the generation of waves, which may prevent convergence. Another reason for possible non-convergence is that non-convergence was actually suggested in a recent numerical investigation for a different variation of the PQG limit: the case of unbalanced or ill-prepared initial conditions [18,19]. For unbalanced initial conditions, the effects of phase changes caused complications. Here, we consider the case of balanced initial conditions—i.e., initial conditions that satisfy geostrophic and hydrostatic balance—and a priori it is unclear whether phase changes will cause non-convergence or not.

The present paper fits into a growing body of mathematical work on moist dynamics, including asymptotic analyses [17–27], rigorous results [28–36], and additional investigations of PQG dynamics and related topics [17–19,37–44].

The remainder of the paper is organized as follows. The model equations and methods are presented in section 2, the numerical investigation of convergence is presented in section 3, and conclusions are summarized in section 4.

2. Model description and methods

This section describes the model of interest—the moist Boussinesq equations—as well as the PQG equations which arise in an asymptotic limit (section 2(a)). Also described are our methods for investigating the convergence in this limit, via numerical simulations (section 2(b)).

(a) Model description

In the investigation here, the starting point is the moist Boussinesq equations, which are described in section 2(a)i. Then an asymptotic limit is described in section 2(a)ii, which is a limit of rapid rotation and strong (moist) stratification, and which leads to the PQG equations.

(i) Moist Boussinesq equations in non-dimensional form

The moist Boussinesq equations, in the non-dimensional form of [17], are

$$\frac{D_h\vec{u}_h}{Dt} + w\frac{\partial\vec{u}_h}{\partial z} + R_0^{-1}\vec{u}_h^{\perp} + E_u\nabla_h\phi = 0, \tag{2.1}$$

$$A^2\left(\frac{D_h w}{Dt} + w\frac{\partial w}{\partial z}\right) + E_u\frac{\partial\phi}{\partial z} - \Gamma A^2 b = 0, \tag{2.2}$$

$$\nabla_h\cdot\vec{u}_h + \frac{\partial w}{\partial z} = 0, \tag{2.3}$$

$$\frac{D_h\theta_e}{Dt} + w\frac{\partial\theta_e}{\partial z} + {Fr_1}^{-2}(\Gamma A^2)^{-1}w = 0, \tag{2.4}$$

$$\frac{D_h q_t}{Dt} + w\frac{\partial q_t}{\partial z} - {Fr_2}^{-2}(\Gamma A^2)^{-1}w - V_r C_{cl}\frac{\partial q_r}{\partial z} = 0, \tag{2.5}$$

where the material derivative has been split into its horizontal part, $D_h/Dt = \partial_t + \vec{u}_h\cdot\nabla_h$, and vertical part, $w\partial_z$, where $\nabla_h = (\partial_x, \partial_y)$ is the horizontal part of the gradient operator. The definition of the buoyancy which appears in (2.2) is

$$b = b_u H_u + b_s H_s, \quad b_u = \theta_e + (R_{vd}\frac{c_p\theta_0}{L_v} - 1)q_t, \quad b_s = \theta_e + (R_{vd}\frac{c_p\theta_0}{L_v} - 1)q_{vs} - \frac{c_p\theta_0}{L_v}(q_t - q_{vs}), \tag{2.6}$$

where H_u, H_s are Heaviside functions that indicate the unsaturated and saturated phases, respectively:

$$H_u = \begin{cases} 1 \text{ for } q_t < q_{vs}, \\ 0 \text{ for } q_t \geq q_{vs}, \end{cases} \qquad \text{and} \qquad H_s = 1 - H_u. \tag{2.7}$$

The other variables that appear in these equations are the horizontal velocity $\vec{u}_h = (u, v)$, the vertical velocity w, the (scaled) pressure ϕ, the equivalent potential temperature θ_e, and the total water mixing ratio q_t. The rain water mixing ratio q_r is defined as the excess water above the saturation value q_{vs}, so that $q_r = \max(0, q_t - q_{vs})$, as in the fast autoconversion and rain evaporation (FARE) microphysics scheme of [10]. In brief, the FARE microphysics scheme is the same as the Kessler warm-rain microphysics, except with the processes of autoconversion, collection, and rain evaporation considered to occur asymptotically fast compared to the dynamical time scales on mesoscales or synoptic scales. The parameter V_r in (2.5) is a non-dimensional version of the fall speed of rain, V_T, and $V_r\,\partial q_r/\partial z$ represents the downward transport of rain.

A main influence of phase changes can be seen in (2.2) and (2.6)–(2.7): the form of the buoyancy is different in unsaturated and saturated phases. This effect is related to latent heating within clouds, which itself can be seen more clearly if the equations are written in terms of potential temperature θ and water vapor mixing ratio q_v, as in (1.1), instead of θ_e and q_t; see [19]. Note that the buoyancy, as defined in (2.6), is continuous but not differentiable at the phase interface, as is consistent with common treatments of phase changes in clouds; while one could possibly use a smoother buoyancy definition, it would likely not cause any significant changes in the numerical solutions here, which already inherently include a smoothing effect due to the finite grid resolution. The most important effect of phase changes is the presence of the two distinct phases and not the details of the smoothness of transition. Other presentations of the moist Boussinesq equations and related systems can be found in past literature [22,45–51], which describe a variety of different settings where phase changes and clouds play an important role. With precipitation included here as part of FARE microphysics, the model in (2.1)–(2.7) follows

[10,17,18,52] most closely. Also note that the model here would reduce to a non-precipitating version of the moist Boussinesq equations by setting $V_r = 0$ and considering q_r to be liquid water q_l. The case of FARE microphysics with $V_r > 0$ is considered here as a simple way to include the effects of precipitation.

Note that the Heaviside functions imply a threshold for the transition between unsaturated and saturated phases, so that no supersaturation is allowed. Also notice that cloud liquid water is included here but no cloud ice. It would be interesting to include supersaturation, more complex warm-rain microphysics, and/or ice microphysics, although it would introduce additional time scales and further complexity to the definition of the distinguished limit, so we focus on the simpler case here for this study of convergence. Some initial considerations in these other directions are described in other studies [17,39,40].

In the non-dimensional equations above, the non-dimensional parameters include the Rossby number Ro, Euler number Eu, aspect ratio A, and buoyancy parameter Γ, which are defined in the appendix of [17] and are analogous to dry Boussinesq parameters [8]. In particular, $\Gamma = BH/W^2$, where $B = g\Theta/\theta_0$, Θ is a characteristic potential temperature fluctuation, and θ_0 is a characteristic (constant) background temperature. Note that the aspect ratio A will be taken to be $O(1)$ below, which differs from the small aspect ratio of synoptic-scale atmospheric flows but is consistent with the use of $A = O(1)$ in rigorous mathematical investigations of the dry QG limit [7,8]. We are unaware of any crucial differences in the dry QG convergence limit between the choices of small and $O(1)$ values of A. For related limits with aspect ratio dependence, see [53].

Due to moisture and phase changes, two Froude numbers appear here, as opposed to the one Froude number of a dry system. A Froude number is associated with each of the two phases (unsaturated and saturated), or, alternatively, as in (2.4)–(2.5), the Froude numbers Fr_1 and Fr_2 are associated with the two thermodynamic variables, θ_e and q_t, respectively. Using traditional definitions, the Froude numbers Fr_u, Fr_s for unsaturated and saturated environments are defined by

$$Fr_u = U/(N_u H), \quad Fr_s = U/(N_s H), \tag{2.8}$$

where U is a characteristic speed, $H = L$ is a characteristic length scale, and N_u, N_s are the respective buoyancy frequencies in each phase. The parameters Fr_1, Fr_2 appearing in the equations (2.4)–(2.5) for θ_e and q_t may be expressed in term of Fr_u, Fr_s using the relationships [18]

$$Fr_u^{-2} = Fr_1^{-2} + Fr_2^{-2}, \qquad Fr_s^{-1} = Fr_1^{-1}, \tag{2.9}$$

so that one could use either the parameters (Fr_u, Fr_s) or (Fr_1, Fr_2) to characterize the system.

(ii) Asymptotic derivation of precipitating quasi-geostrophic equations

The asymptotic limit of interest is a limit of rapid rotation and strong (moist) stratification. In terms of the non-dimensional parameters, this limit is characterized by small Rossby and Froude numbers, respectively. The distinguished limit which relates the non-dimensional parameters is

$$Ro = Eu^{-1} = \epsilon, \quad Fr_1 = O(\epsilon), \quad Fr_2 = O(\epsilon), \quad \Gamma A^2 = {Fr_1}^{-1}, \quad \frac{c_p \theta_0}{L_v} = O(\epsilon), \tag{2.10}$$

where the latent heat of vaporization L_v is one of the new parameters associated with phase changes, and where the Rossby number has been identified as the small parameter ϵ.

Using this asymptotic scaling and distinguished limit, the model in (2.1)–(2.6) becomes

$$\frac{D_h \vec{u}_h}{Dt} + w\frac{\partial \vec{u}_h}{\partial z} + \epsilon^{-1}\vec{u}_h^{\perp} + \epsilon^{-1}\nabla_h \phi = 0, \tag{2.11}$$

$$\frac{D_h w}{Dt} + w\frac{\partial w}{\partial z} + \epsilon^{-1}\frac{\partial \phi}{\partial z} = \epsilon^{-1} b, \tag{2.12}$$

$$\nabla_h \cdot \vec{u}_h + \frac{\partial w}{\partial z} = 0, \tag{2.13}$$

$$\frac{D_h\theta_e}{Dt} + w\frac{\partial\theta_e}{\partial z} + \epsilon^{-1}w = 0, \tag{2.14}$$

$$\frac{D_h q_t}{Dt} + w\frac{\partial q_t}{\partial z} - \epsilon^{-1}w - V_r\frac{\partial q_r}{\partial z} = 0, \tag{2.15}$$

along with the buoyancy definition,

$$b = \begin{cases} \theta_e + (\epsilon - 1)\, q_t & \text{if} \quad q_t < q_{vs}, \\ \theta_e + (\epsilon - 1)\, q_{vs} - \epsilon(q_t - q_{vs}) & \text{if} \quad q_t \geq q_{vs}. \end{cases} \tag{2.16}$$

Note that the additional specifications of $A = 1$, $C_{cl} = 1$, and $Fr_1 = Fr_2$ have also been used, in order to simplify notation and arrive at a system where each coefficient is either 1 or ϵ. The derivation follows previous work [17–19] in which further details are described. Also note that we leave $V_r = 0$, $V_r = O(1)$ or $V_r = O(\epsilon^{-1})$ to be specified, since we consider different scenarios for dimensional rainfall speed V_T: no rainfall, or moderate speed $V_T = 0.1$ m/s or large speed $V_T = 1$ m/s, respectively. The case of large speed will lead to a different type of PQG dynamics and is left as future work, while the two cases of $V_r = 0$ and $V_r = 1$ are considered here.

A new aspect of PQG asymptotics is that moisture and phase changes are an inherent and interactive part of the dynamics in the model in (2.11)–(2.16) and in the distinguished limit in (2.10). This aspect was one goal of the PQG derivation of [17], in moving beyond past frameworks of moist QG equations [11–16] that treat moisture and/or latent heating as a supplement or add-on to the dry QG equations. A PQG derivation could be carried out using more comprehensive cloud microphysics [17,39,40] using the same general ideas described here, although we use the moist Boussinesq system in (2.1)–(2.7) as a simple choice that includes the main features of phase changes and precipitation.

The main steps of the derivation of the PQG equations are now briefly described. All variables are expanded as asymptotic series in powers of ϵ as

$$f = f^{(0)} + \epsilon f^{(1)} + \epsilon^2 f^{(2)} + \cdots \tag{2.17}$$

where $f(\vec{x}, t)$ is used as a stand-in for all model variables: $u, v, w, \phi, \theta_e, q_t$, etc. The dominant balance of (2.11)–(2.16) at $O(\epsilon^{-1})$ is seen to be

$$u^{(0)} = -\frac{\partial\psi}{\partial y}, \qquad v^{(0)} = \frac{\partial\psi}{\partial x}, \qquad b^{(0)} = \frac{\partial\psi}{\partial z}, \qquad \xi^{(0)} = \nabla_h^2\psi, \qquad w^{(0)} = 0, \tag{2.18}$$

where the notation $\psi = \phi^{(0)}$ has been used to introduce the streamfunction ψ. The leading-order expression for the buoyancy is

$$b^{(0)} = H_u b_u^{(0)} + H_s b_s^{(0)}, \quad b_u^{(0)} = \theta_e^{(0)} - q_t^{(0)}, \quad b_s^{(0)} = \theta_e^{(0)} - q_{vs}. \tag{2.19}$$

The leading-order balances in (2.18) represent geostrophic and hydrostatic balance, along with the introduction of ξ as the vertical component of the total vorticity $\nabla \times \vec{u}$.

Beyond the balance conditions in (2.18) which arise at $O(\epsilon^{-1})$, the dynamical evolution equations would arise at the next order at $O(\epsilon^0)$. Rather than taking this route to the dynamical equations, another common approach is to proceed by seeking dynamical quantities with slow evolution—i.e., quantities whose evolution equations do not involve any fast ϵ^{-1} terms [8]. To follow this route, we inspect (2.14) and (2.15) and notice that the fast terms $\epsilon^{-1}w$ can be eliminated from the θ_e and q_t evolution equations by using the linear combination

$$M = q_t + \theta_e, \tag{2.20}$$

which evolves according to

$$\frac{DM}{Dt} = V_r\frac{\partial q_r}{\partial z}, \tag{2.21}$$

where $D/Dt = \partial/\partial t + \vec{u}\cdot\nabla$ is the three-dimensional material derivative. Since (2.21) involves no fast ϵ^{-1} terms (if $V_r = O(1)$), the quantity M is called a slow variable, and (2.21) will provide one evolution equation for the PQG equations in the limit $\epsilon \to 0$.

A second slow quantity is the potential vorticity variable defined as

$$PV_e = \xi + \frac{\partial \theta_e}{\partial z}, \tag{2.22}$$

where ξ is the vertical component of the total vorticity $\nabla \times \vec{u}$. To find the evolution equation for PV_e, take the curl of the horizontal momentum equation from (2.11), and then add the result to the z-derivative of the θ_e-equation in (2.14), which leads to

$$\frac{\partial PV_e}{\partial t} + \frac{\partial \left(\vec{u} \cdot \nabla \theta_e\right)}{\partial z} + NL_\xi = 0, \tag{2.23}$$

where a group of nonlinear terms has been defined as

$$NL_\xi = \nabla_h \times \left(\vec{u}_h \cdot \nabla_h \vec{u}_h + w \frac{\partial \vec{u}_h}{\partial z} \right) = \vec{u} \cdot \nabla \xi + \xi(u_x + v_y) + (w_x v_z - w_y u_z). \tag{2.24}$$

In terms of the material derivative of PV_e, the evolution equation can be written as

$$\frac{DPV_e}{Dt} = -\vec{u}_z \cdot \nabla \theta_e - \xi(u_x + v_y) - (w_x v_z - w_y u_z). \tag{2.25}$$

Since (2.25) involves no fast ϵ^{-1} terms, the variable PV_e is considered a slow quantity, and (2.25) will provide a second evolution equation for the PQG equations in the limit $\epsilon \to 0$.

Finally, to arrive at the evolution equations for the PQG model, the asymptotic expansion in (2.17) is inserted into the M and PV_e evolution equations in (2.21) and (2.25), respectively. Then the leading-order balances from (2.18) are used to find

$$\frac{D_0}{Dt} M^{(0)} = V_r \frac{\partial q_r^{(0)}}{\partial z}, \tag{2.26}$$

$$\frac{D_0}{Dt} PV_e^{(0)} = -\vec{u}_z^{(0)} \cdot \nabla \theta_e^{(0)}, \tag{2.27}$$

to leading order in ϵ. The advection operator here is $D_0/Dt = \partial/\partial t + \vec{u}^{(0)} \cdot \nabla$, where $\vec{u}^{(0)} = (u^{(0)}, v^{(0)}, 0)$. These advection operators are one difference between the evolution equations for (M, PV_e) in the Boussinesq case in (2.21) and (2.25) versus the PQG case in (2.26)–(2.27): in the PQG case, the advection is purely horizontal, since $w^{(0)} = 0$. A second difference is in the right-hand side of the PV_e evolution equations: the PQG PV_e evolution in (2.27) does not include the last terms of the Boussinesq PV_e evolution in (2.25), since $w^{(0)} = 0$ and $u_x^{(0)} + v_y^{(0)} = 0$. Hence, if the balance conditions in (2.18)–(2.19) are satisfied, then the Boussinesq evolution equations will become the PQG evolution equations in (2.26)–(2.27).

In comparing the PQG system to the traditional dry QG equations, an important distinction is that two dynamical equations (2.26) and (2.27) (for M and PV_e) are needed for the PQG equations, whereas only one dynamical equation (for PV) is needed for the dry QG equations. One should also take note of the right-hand-side of the evolution equation for PV_e: in (2.27) the term $\vec{u}_z \cdot \nabla \theta_e$ does not vanish for the PQG equations. It does vanish in the saturated phase, since θ_e is proportional to the buoyancy, so that the term is proportional to $(\vec{k} \times \nabla \psi_z) \cdot \nabla \psi_z \equiv 0$ as can be seen from (2.18)–(2.19), but it does not vanish in the unsaturated phase, since θ_e is not proportional to the buoyancy in the unsaturated phase. Physically, the non-vanishing of the $\vec{u}_z \cdot \nabla \theta_e$ term represents the impact of phase changes on PV evolution.

(b) Numerical assessment methods

Here we explain the set-up of our numerical simulations and the techniques used to assess convergence or non-convergence to the PQG equations. Specifically, the goal is to monitor the growth of waves (or lack thereof). To do so, the vertical velocity w is tracked in time, as an indicator of wave activity. The departures from geostrophic and hydrostratic balance (2.18) are complementary quantities to assess how well balance is maintained over time, for different values of ϵ. We also measure the nonlinear terms $\xi(u_x + v_y) - (w_x v_z - w_y u_z)$ in the PV_e-equation (2.25),

which should remain $O(\epsilon)$ in amplitude for $O(1)$ times, as numerical verification that PV_e is a balanced variable.

(i) Numerical Method

The 3D moist Boussinesq equations with two phases of water (vapor and liquid) are simulated in a 2π-periodic domain using a dealiased, pseudo-spectral code. Calculations with spatial resolutions $128 \times 128 \times 128$ and $256 \times 256 \times 256$ are compared to ensure that the results are insensitive to resolution. The comparison provides confidence in the robustness of our results, especially for the smallest value of the Rossby and Froude numbers ($\epsilon \sim 10^{-3}$).

After transferring the physical space equations into Fourier space, a third-order Runge-Kutta time-stepping scheme solves the coupled system of ODEs resulting from discretization of the wavevector. The rotation and buoyancy terms are treated explicitly, and the nonlinear advection terms are calculated in physical space with the discrete Fourier transform algorithms of the FFTW software package (http://www.fftw.org/). A pressure-solver enforces the incompressibility constraint, and viscous linear terms are included using an integrating factor. A hyperviscosity is used instead of the normal viscosity to induce dissipation only at the smallest scales. For example, in the momentum equation, the hyperviscosity takes the form

$$(-1)^{p+1}\nu(\nabla^2)^p\vec{v}, \tag{2.28}$$

where we use $p = 8$. The coefficient ν has the structure

$$\nu = 2.5\left(\frac{E_\nu(k_m,t)}{k_m}\right)^{1/2} k_m^{2-2p}, \tag{2.29}$$

where k_m is the highest available wavenumber and E_ν is the kinetic energy in the wavenumber shell associated with k_m. The spherical shell associated with wavenumber k_i includes all wavenumbers satisfying $(i-1)\Delta k < (\vec{k}\cdot\vec{k})^{1/2} \le i\Delta k$, $\Delta k = (2\pi)/L$, and L is length of the box (in our case $L = 2\pi$), where $i = 1 \cdots N$ (e.g., in the 128^3 spatial resolution case, $N = 43$ because of the $2/3$-rule for dealiasing).

(ii) Discussion of Time Scales

The model equations have been nondimensionalized so that $t = O(\epsilon)$ is closely linked to the fast waves (time scale τ), while $t = O(1)$ is associated with slow motions (time scale t). Time steps in the numerical simulations are chosen small enough to satisfy the CFL condition, and simultaneously to resolve the fast-wave oscillations. For the CFL condition, the time step Δt satisfies $\Delta t = \dfrac{\mathrm{CFL}}{|\vec{u}|_m k_m}$, where k_m is the highest available wavenumber, $|\vec{u}_m|$ is the maximum magnitude of the velocity field and CFL = 0.9. To resolve the waves, each half-period is sampled at least 5 times, according to the condition $\Delta t = \dfrac{\pi}{5\sigma_{max}}$, where σ_{max} is the maximum frequency of the waves. We consider the special case $Fr_1 = Fr_2 = Ro = \epsilon$ corresponding to $(Fr_u, Fr_s) = (\epsilon/\sqrt{2}, \epsilon)$ with $\epsilon = (10^{-3}, 10^{-2}, 10^{-1})$. Thus the maximum wave frequency is $\sigma_{max} = \sqrt{2}\epsilon^{-1}$ [19]. After calculating Δt based on the CFL and wave conditions, we select the smaller of the two time steps. The values of (Ro, Fr_u, Fr_s) are defined in terms of a characteristic velocity magnitude, which we select based on the initial condition. At later times, as the velocity field evolves, a different characteristic velocity value could emerge. Therefore, we monitor the evolution in time of the Froude and Rossby numbers by calculating the values of these non-dimensional quantities based on their definitions in Table A2 of [17], where $L = H = 2\pi$ and U is the maximum magnitude of the velocity field. During $O(1)$ time intervals of our decay simulations with hyperviscosity, the values of (Ro, Fr_u, Fr_s) do not change significantly (e.g., if $Ro = 10^{-1}$ initially, then at later times $Ro = 10^{-1} + O(10^{-2})$), so the value of ϵ based on the initial conditions is a stable indicator for the relative time scales associated with rotation/stratification compared to the time scale of nonlinear advection.

(iii) Balanced Initial Conditions

Here we explain how to generate balanced initial conditions. To do so, we begin from a state (u, v, w, θ_e, q_t) with waves present, since such a state is easiest to generate, and then we remove the wave component. To remove the waves, we use PV-and-M inversion [17,44], which is a moist analog of dry PV inversion. The inversion process starts from the fields for (M, PV_e), which can be found from (u, v, w, θ_e, q_t) using (2.20) and (2.22). The values of (M, PV_e) then enter as parameters into the following partial differential equation (PDE) for balanced streamfunction ψ:

$$\nabla_h^2\psi + \frac{\partial}{\partial z}[H_u(\frac{1}{2}\frac{\partial\psi}{\partial z} + \frac{1}{2}M)] + \frac{\partial}{\partial z}[H_s(\frac{\partial\psi}{\partial z} + q_{vs})] = PV_e, \tag{2.30}$$

which determines the slow components $\vec{u}_{(M,PV_e)}$, $\theta_{e(M,PV_e)}$ and $q_{t(M,PV_e)}$ in terms of ψ:

$$\vec{u}_{(M,PV_e)} = \left(-\frac{\partial\psi}{\partial y}, \frac{\partial\psi}{\partial x}, 0\right), \quad \theta_{e(M,PV_e)} = \frac{1}{2}H_u\left(\frac{\partial\psi}{\partial z} + M\right) + H_s\left(\frac{\partial\psi}{\partial z} + q_{vs}\right), \tag{2.31}$$

$$q_{t(M,PV_e)} = M - \theta_{e(M,PV_e)}.$$

The nonlinear, elliptic PDE in (2.30) follows from the definitions (2.20), (2.22) of (M, PV_e); the geostrophic and hydrostatic balance relations (2.18); and the relations (2.19) for buoyancy b in terms of θ_e, q_t in the limit $\epsilon \to 0$. The PDE is nonlinear [17,44] because the Heaviside functions H_u and H_s are functions of $q_{t(M,PV_e)}$ which itself is a function of ψ according to (2.31). To solve the nonlinear PDE, an iterative procedure is used. First, an initial guess is used for (H_u, H_s), which are then frozen momentarily so that (2.30) becomes a linear PDE (with discontinuous coefficient in front of the $\partial\psi/\partial z$ term). Solving the linear PDE provides estimates of the balanced/slow components, which helps to filter out the fast waves from the original initial conditions. The estimate for $q_{t(M,PV_e)}$ is then used to determine a new guess for (H_u, H_s), and the procedure repeats. One can check consistency by comparing the new guess for (H_u, H_s) and the previous guess for (H_u, H_s); if they are not the same, the procedure is iterated until convergence.

The function that is used as the initial condition should have variations on large scales only (characterized by the Rossby deformation radius), in order to be consistent with PQG scaling assumptions. To select such a function, we use a superposition of sinusoids (i.e., a Fourier series) including only wavenumbers 1 through 5. To make the initial condition a generic function, the Fourier coefficients are treated as independent Gaussian random variables with mean zero and with the variance for each wavenumber assigned according to the spectral density function

$$F(k) = \epsilon_f \frac{\exp(-0.5(k-k_f)^2/s^2)}{(2\pi)^{1/2}s}, \qquad \text{for} \quad k \in [1, 5], \tag{2.32}$$

where $s = 1$ characterizes the spread in k-space, $k_f = 3$ is the peak wavenumber and ϵ_f is an $O(1)$ coefficient. The horizontal mean flows $(\bar{u}, \bar{v})$ corresponding to $k_h = 0$ will also be present in general. Such a random function is selected for each of the variables (u, v, w, θ_e, q_t), and then the wave component is removed as described above. The results will be presented below for one particular randomly selected initial condition; robustness was verified by running three additional simulation sets with different randomly selected initial conditions, with a resolution of 128^3 for the the standard setup case, and the convergence results were essentially the same for all of these initial conditions.

(iv) Cloud Fraction

The cloud fraction will be one parameter that we vary in order to assess different dynamical scenarios. In order to set the cloud fraction for a simulation, we use the saturation parameter q_{vs}. According to the formulas $q_v = \min(q_t, q_{vs})$, $q_l = \max(0, q_t - q_{vs})$, larger values of the saturation threshold q_{vs} correspond to smaller cloud fractions. The values chosen for comparison are $q_{vs} = 10, 0.5, 0, -0.5$, such that we obtain cloud fractions increasing from, respectively, 0%, 22%, 50% to 76%. Since cloud fraction is actually a dynamical, evolving quantity, during the flow evolution, we continue to monitor q_v, q_l, and the cloud fraction is calculated as the L^1 norm of the cloud

indicator $H_s(q_t - q_{vs})$. We find that the fluctuations of $||H_s||_1$ are small on $O(1)$ time scales, so it is reasonable to use the initial value of cloud fraction $||H_s(q_t - q_{vs})||_1$ to characterize the physical setting of each simulation.

3. Results of numerical simulations

In this section, numerical simulations are used to test the convergence to precipitating quasi-geostrophic equations with phase changes. The focus will be the scenario where the initial conditions are balanced (section 2(b)(iii)). First, in section 3(a), we show illustrations of the system's evolution, and distinguish between the fast-time and slow-time evolution. Then, in section 3(b), statistics are analyzed to assess whether the fast-time-scale waves converge to zero as $\epsilon \to 0$. Finally, some additional sensitivity studies will be described to assess the impact of different cloud fractions and different fall speed of rain.

(a) A first assessment: visualization of the evolution

Before analyzing any statistical measures of convergence, we first consider some illustrations to visualize the behavior of the system, and to see if the illustrations are consistent with convergence to balanced (PQG) dynamics. The illustrations are shown for the case with cloud fraction $||H_s(q_t - q_{vs})||_1 = 50\%$, and $V_r = 0$ such that liquid water does not fall. Since the full Boussinesq system includes both fast waves and more slowly evolving components, we will view the evolution over both short and long time scales.

The short-time evolution is shown in Figure 1. The variables shown are zonal velocity u (first row), vertical velocity w (second row), total water q_t (third row), and the Heaviside function H_s as a cloud indicator (fourth row). In this plot, the moist Boussinesq system in (2.11) - (2.16) is evolving in a 3D triply periodic domain with $\epsilon = O(0.1)$, and the plot shows a 2D slice in the $y = \pi$ plane. To illustrate the short-time evolution on the time scale of the waves, the snapshots are shown at times $t = 0, 0.1$, and 0.2 in the left, middle, and right columns, respectively, which correspond to times $t = 0, \epsilon$, and 2ϵ since $\epsilon = 0.1$. Notice that the initial condition of w is zero, since the initial condition is balanced (see section 2(b)iii). The vertical velocity w can be viewed as an indicator of the degree of imbalance and the amount of wave activity. As time evolves, in Figure 1, one can see that w fluctuates substantially on these short time scales, which indicates that waves have been generated. Nevertheless, the magnitude of w is small, which indicates that the system is still nearly balanced. The other variables shown, u and q_t, appear to the eye to remain almost the same from time to time on these short time scales, which is another indication that the system is nearly balanced.

Figure 2 shows the long-time evolution at times $t = 0, 1$, and 2, which are $O(1)$ times and are considered long time scales compared to the short time scale of the fast waves. The setup of the figure is otherwise the same as in Figure 1. In contrast to figure 1, where u and q_t change very little on short time scales, the variation of u and q_t are much more significant over the longer time scales from $t = 0, 1$, and 2. If this case with $\epsilon = 0.1$ is close to convergence in the $\epsilon \to 0$ limit, then u and q_t would be evolving approximately according to the PQG equations (although the plots show solutions to the moist Boussinesq equations with $\epsilon = 0.1$). As one indication of convergence to PQG dynamics, notice that the magnitude of w remains small at times $t = 1$ and 2. The small w is an indication that the leading-order balance condition, $w^{(0)} = 0$ in (2.18), is approximately satisfied. Hence, Figures 1 and 2 are consistent with convergence toward PQG dynamics, as a first assessment based on the single value of $\epsilon = 0.1$.

(b) Statistical studies and sensitivity tests

In moving beyond the illustrations of $\epsilon = 0.1$ in Figures 1–2, we now consider statistical measures, and we consider a sequence of decreasing values of $\epsilon = 0.1, 0.01$, and 0.001.

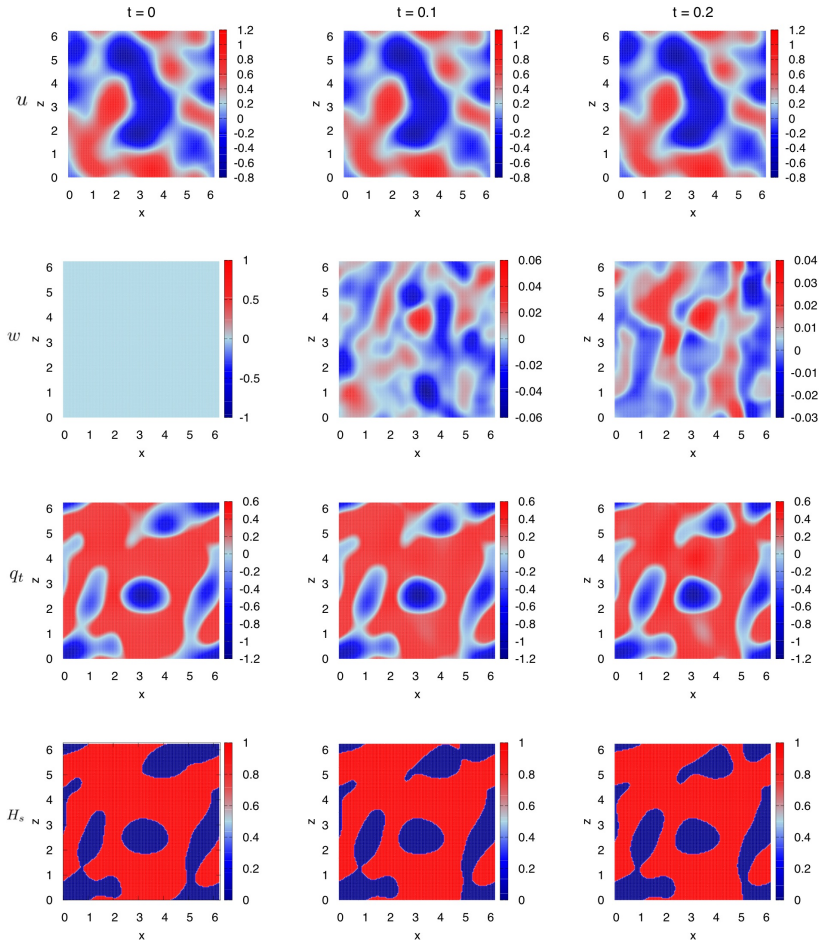

Figure 1. Short-time evolution of u (first row), w (second row), q_t (third row) and H_s (fourth row) on short times of $t = O(\epsilon) \sim 10^{-1}$, starting from balanced large-scale random initial conditions at $t = 0$. The 2D slices are taken with $y = \pi$ held fixed. Note that the cloud indicator H_s takes discrete values of 1 or 0 for the presence or absence of cloud, respectively. One can see that u and q_t, which are balanced at the initial time $t = 0$, change very little over short times $t = O(\epsilon)$. On the other hand, as an indicator of waves, w evolves on this short time scale, but its magnitude remains at $O(\epsilon)$ level.

Figure 3 shows the results of numerical simulations with small ϵ, and for selected quantities that are expected to decrease as ϵ is reduced, if there is convergence from the Boussinesq system to a quasi-geostrophic system. The representative quantities are the vertical velocity w (top panels), the horizontal component of geostrophic imbalance $v - \phi_x$ (bottom left), and the nonlinear terms $\xi(u_x + v_y) - (w_x v_z - w_y u_z)$ in the PV_e-equation (2.25) (bottom right). The blue color indicates data from simulations with cloud fraction 50% and phase changes. The red color indicates data from baseline, purely unsaturated simulations with only water vapor ($H_u = 1$ and $H_s = 0$ everywhere). In the latter case, the equations are equivalent to the dry system by a change of variables, and thus convergence results are known from past literature [7,8].

We first draw attention to the time dependence associated with the L^2 norm of vertical velocity, seen in the top left panel ($\epsilon = 0.1$, resolution 256^3). In both saturated and phase-change simulations, fast oscillations are immediately generated for $t > 0$ during an initial adjustment phase. This is consistent with generation of waves by nonlinear interactions and/or higher-order

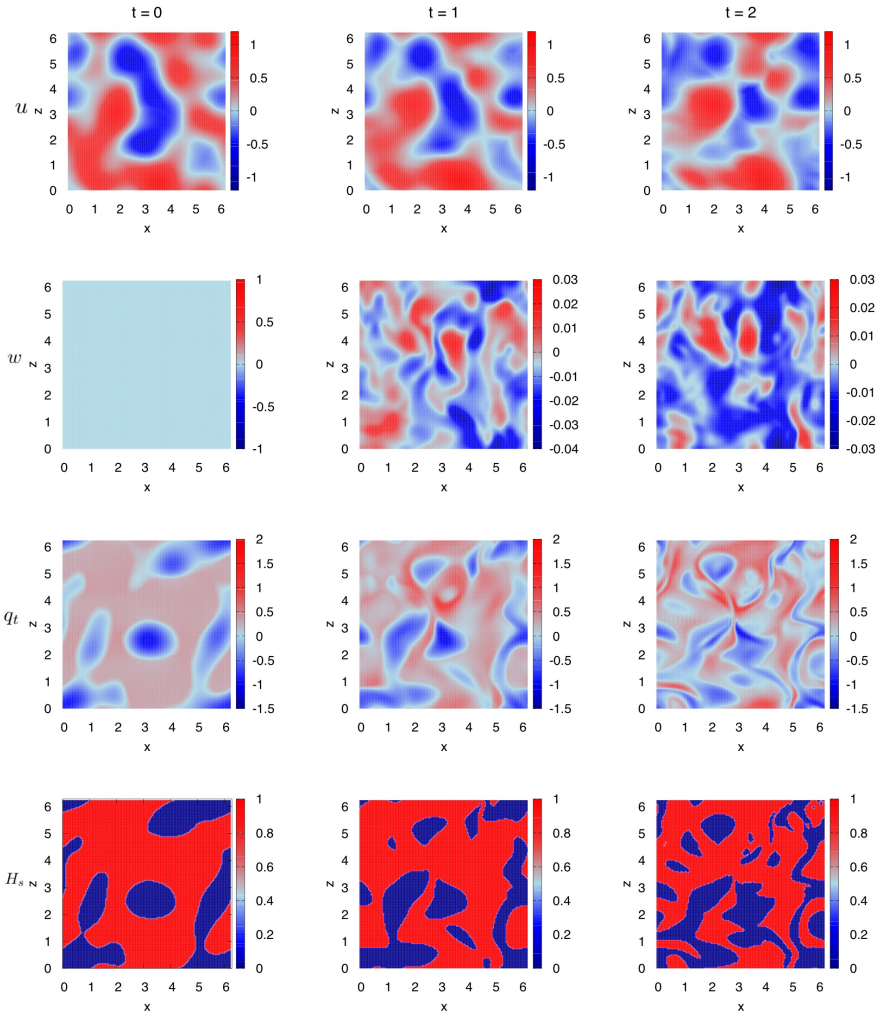

Figure 2. Long-time evolution of horizontal velocity u (first row), vertical velocity w (second row), total water q_t (third row) and cloud indicator H_s (fourth row). The simulation is the same as in figure 1, and 2D slices have $y = \pi$ held fixed. Note that the cloud indicator H_s takes discrete values of 1 or 0 for the presence or absence of cloud, respectively. The saturation threshold $q_{vs} = 0$, such that, in the q_t plots, red corresponds to liquid water and blue corresponds to water vapor. The variables u and q_t are evolving on these longer time scales from $t = 0$ to $t = 1$ to $t = 2$. The magnitude of w remains small, consistent with the balance conditions in (2.18) in the PQG limit.

imbalance [54–58]. For small times $O(\epsilon)$, the amplitude of the oscillations is roughly a factor of 2 larger when phase changes are present. However, their magnitude decreases until $t \approx 5$, after which time the L^2 norm of w is approximately the same for both cases. Notice that beyond $t \approx 5$, the vertical velocity is 10 times smaller than ϵ and roughy 50 times smaller than horizontal velocities (figure 2). All fields decay slowly after $t = O(1)$ under the action of hyperviscosity.

The remaining panels in figure 3 show L^2 norms of w; $v - \phi_x$; $\xi(u_x + v_y) - (w_x v_z - w_y u_z)$ vs. ϵ, on a log-log scale, and at fixed time $t = 0.4$ (top right and bottom panels). The time $t = 0.4$ is chosen as an $O(1)$ time scale with respect to the limit $\epsilon \to 0$, and it is a computationally feasible end time for the most expensive simulation of $\epsilon = 10^{-3}$. Given that w remains essentially the same order of magnitude at many times (see figure 3, upper left panel), we consider $t = 0.4$ as a representative time and do not address relatively small changes in the results arising

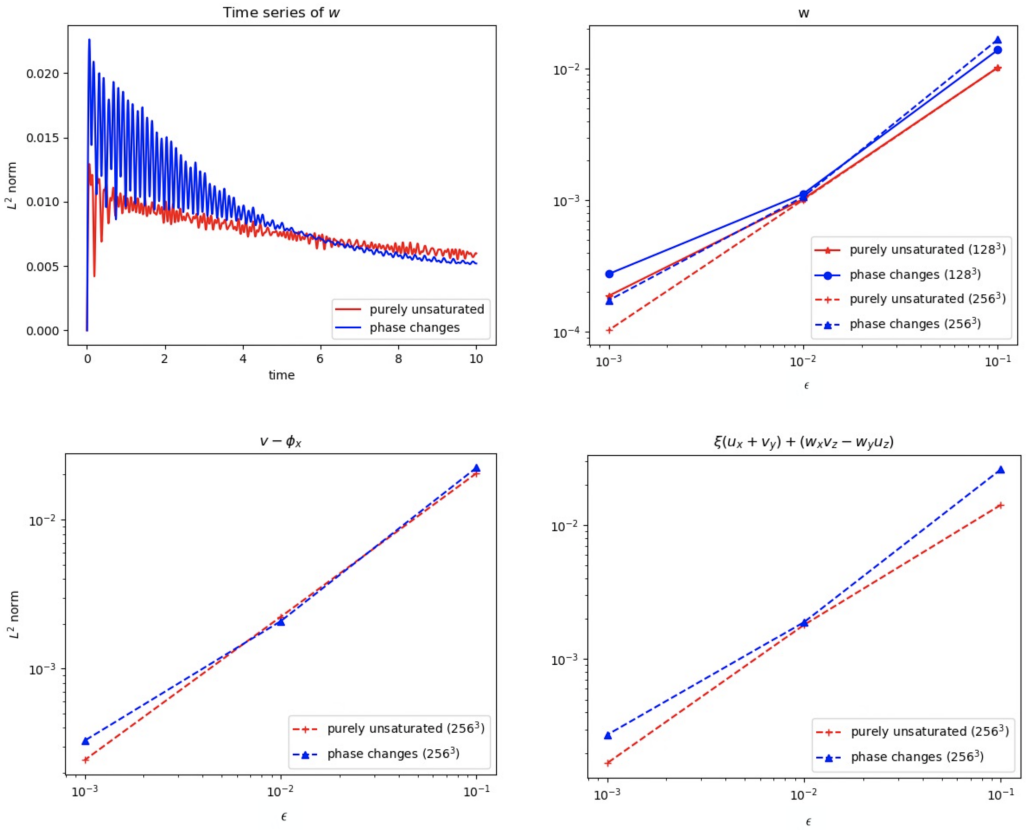

Figure 3. Statistical assessment of convergence or non-convergence. Top Left: the L^2 norm of vertical velocity vs. time (fixed $\epsilon = 0.1$, resolution 256^3). Top Right: the L^2 norm of vertical velocity vs. $\epsilon = 10^{-3}, 10^{-2}, 10^{-1}$ (fixed time $t = 0.4$, resolutions $128^3, 256^3$). Bottom Left: the L^2 norm of the horizontal component of geostrophic imbalance vs. $\epsilon = 10^{-3}, 10^{-2}, 10^{-1}$ (fixed time $t = 0.4$, resolution 256^3). Bottom Right: the L^2 norm of nonlinear terms in the PV_e-equation (2.25) (other information is the same as bottom left). Red symbols are data from the unsaturated case with only water vapor, and blue symbols are data from the simulation with phase changes (cloud fraction 50%, $V_r = 0$). Solid lines (dashed lines) connect data points found for resolution 128^3 (256^3). In all cases, flows evolve from balanced, large-scale, random initial conditions.

from small changes in the measurement time. Solid lines (dashed lines) connect data points for $\epsilon = (10^{-1}, 10^{-2}, 10^{-3})$ found with resolution 128^3 (256^3). These data points are used to provide intuition regarding convergence to balance as $\epsilon \to 0$, and rate of convergence is assessed only in an approximate sense.

The saturated simulations (red symbols) are the benchmark for comparison, since it is known that balance is achieved to $O(\epsilon)$ for times $t = O(1)$ [7,8]. This case also helps to establish any sensitivity of the results to the resolution in terms of Fourier modes. For the L^2 norm of vertical velocity (top right), there is a comparison between resolutions 128^3 (solid) and 256^3 (dashed). Focusing on the red symbols, one can see resolution dependence for the lowest value of $\epsilon = 10^{-3}$, but the convergence is well approximated even with 128^3 Fourier modes.

Next we turn to the blue curves on the top right and bottom panels of figure 3, to assess the possibility for convergence of the Boussinesq system to the PQG equations in (2.18)–(2.19) and (2.26)-(2.27) in the presence of phase changes. Similar to the unsaturated case, it is evident that departures from balance are diminishing with a trend that suggests convergence to PQG as $\epsilon \to 0$. Summarizing, figure 3 shows that balance is approximately achieved at $O(1)$ times in the

evolution from balanced initial conditions for $10^{-3} \leq \epsilon \leq 10^{-1}$, with and without phase changes, and wave activity is roughly an order of magnitude smaller than ϵ in the L^2 sense.

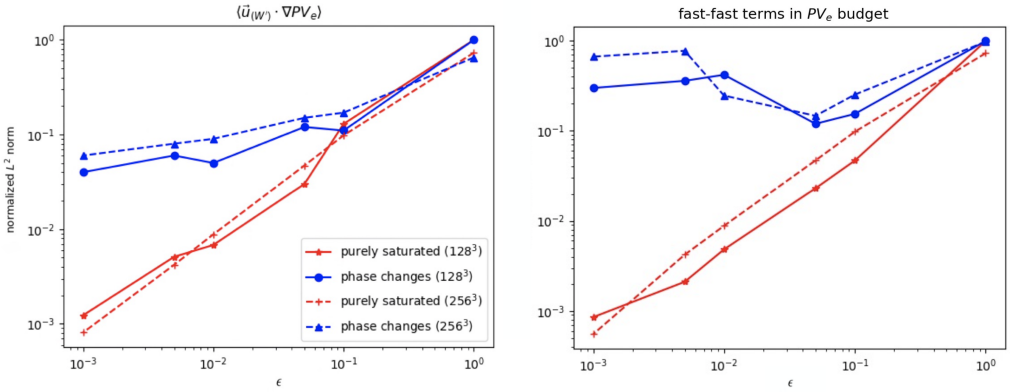

Figure 4. Dependence on ϵ of the L^2 norm of $\langle \vec{u}_{(W')} \cdot \nabla PV_e \rangle$ (left) and $\langle -\vec{u}_{(W')} \cdot \nabla (\theta_e)_{(W')} - \xi_{(W')} w_{z(W')} + w_{x(W')} v_{z(W')} - w_{y(W')} u_{z(W')} \rangle$ (right), for unbalanced initial conditions with waves present. These are two of the wave-coupling terms in the fast-wave-averaged equation for PV_e, where the angle brackets $\langle \cdot \rangle$ denote a time-average over $O(1)$ times. For purely saturated dynamics (red), the magnitudes decay roughly linearly with decreasing ϵ. In contrast, the decrease with ϵ is significantly slower in the simulations with phase changes (blue), and will perhaps remain nonzero as $\epsilon \to 0$. For simulations with phase changes, the cloud fraction is 22% and the rainfall parameter $V_r = 0$. The purely saturated simulations have liquid water everywhere. Reprinted with permission from [19].

Figure 3 pertains to convergence of the Boussinesq system (2.11)-(2.16) to the PQG equations in (2.18)–(2.19) and (2.26)-(2.27), starting from well-prepared initial data in the absence of waves, but one can also consider more general initial conditions. A general initial condition could include contributions from waves and it is then called an ill-prepared or unbalanced initial condition. Starting from unbalanced initial conditions with waves, Figure 4 shows a time average of terms in the full, nonlinear evolution equation for PV_e. Here the initial energy is again large-scale and randomly distributed, but with roughly equal parts in slow modes (M, PV_e) and fast waves. To explain this plot, we first briefly review some relevant literature on the dry Boussinesq system with ill-prepared initial data.

For unbalanced initial conditions, the fast-wave averaging framework involves a budget analysis of time-averaged terms in the (M, PV_e)-equations (2.21) and (2.25), wherein interactions between slowly varying modes and fast waves are averaged on $O(1)$ (slow) times in the limit $\epsilon \to 0$ [8,18,19,59–61]. Following a change of variables [18], all fields are decomposed into their slow (M, PV_e) and fast (W') parts, for example, the velocity vector $\vec{u} = \vec{u}_{(M,PV_e)} + \vec{u}_{(W')}$. After substitution of decomposed fields into the (M, PV_e) equations, the time evolution of (M, PV_e) is governed by terms that can be classified as slow-slow, slow-fast, fast-slow and fast-fast. For example, in figure 4, $\langle \vec{u}_{(W')} \cdot \nabla PV_e \rangle$ (left panel) is a fast-slow term because $\vec{u}_{(W')}$ is fast and ∇PV_e is slow, and the angle brackets denote the average over $O(1)$ times. Physically, the term $\langle \vec{u}_{(W')} \cdot \nabla PV_e \rangle$ represents advection of slow PV_e by the fast-wave component of velocity. The fast-fast terms in the PV_e budget $\langle -\vec{u}_{(W')} \cdot \nabla (\theta_e)_{(W')} - \xi_{(W')} w_{z(W')} + w_{x(W')} v_{z(W')} - w_{y(W')} u_{z(W')} \rangle$ (right panel) involve products of two fast components, originating from the right-hand-side of (2.25). The fast-fast terms in the PV_e-evolution equation measure direct feedback from waves onto the slow PV_e variable.

In single-phase dynamics (dry, purely unsaturated or purely saturated), and in the limit $\epsilon \to 0$, the vortical component of Boussinesq dynamics evolves separately from the waves [7,8,18,53,59–63]. The latter statement is true for evolution starting from either balanced or unbalanced initial

conditions, and has been proved rigorously [7,8,53,59–63]. For unbalanced initial conditions, a numerical demonstration for saturated dynamics is shown by the red data points in figure 4, using $10^{-3} \leq \epsilon \leq 1$ (reproduced with permission from [19]). These data points show that, in the equation for the slow PV_e, the wave-coupling terms decrease in proportion to ϵ. On the other hand, when waves are initially present and phase changes occur during the evolution, the blue data points suggest that coupling to waves may persist even as $\epsilon \to 0$ [18,19].

The blue data in figures 3 and 4 should be contrasted with each other, both for simulations with phase changes present. Figure 3 suggests vanishing wave activity and convergence to PQG for balanced initial conditions, while figure 4 suggests sustained wave-coupling for unbalanced initial conditions. In particular, figure 3 (bottom right) for balanced initial conditions shows almost-linear decrease with ϵ of nonlinear terms in the full PV_e-evolutions equation (2.25), indicating convergence to the PQG equation (2.27). On the other hand, for the unbalanced initial conditions of figure 4 (right), the fast-fast part of the right-hand-side of (2.25) remains $O(1)$ for our lowest $\epsilon = 10^{-3}$. Thus the Boussinesq PV_e dynamics evolving from unbalanced initial conditions has terms beyond the balanced PQG system (2.26)-(2.27).

Returning to evolution from balanced initial conditions, as in figure 3, it is natural to ask about the robustness of the convergence results. For instance, does rainfall have any impact on the outcome? How do the results depend cloud fraction? To answer these questions, we performed additional simulations at resolution 128^3 modes, with selected data displayed in figure 5. In particular, we focus on the L_2 norm of the vertical velocity as an indicator of wave activity.

To explore the effect of rainfall, we ran a simulation with $V_r = 1$ (figure 5 left) and compared the L_2 norm of w to our previous case with $V_r = 0$ (figure 3 top). In both simulations, the initial cloud fraction is 50%. Also shown in figure 5 (left) is the purely unsaturated simulation with cloud fraction 0% (water vapor only). For $\epsilon = 10^{-1}$ and 10^{-2}, the results for $V_r = 0$ and $V_r = 1$ are approximately the same to the eye, with a difference only at the smallest value $\epsilon = 10^{-3}$, which was earlier noted to be sensitive to a change in resolution from 128^3 to 256^3 Fourier modes. Thus, the simulations suggest convergence to PQG in the presence of phase changes *and* rainfall, albeit possibly slower for $V_r = O(1)$ compared to $V_r = 0$.

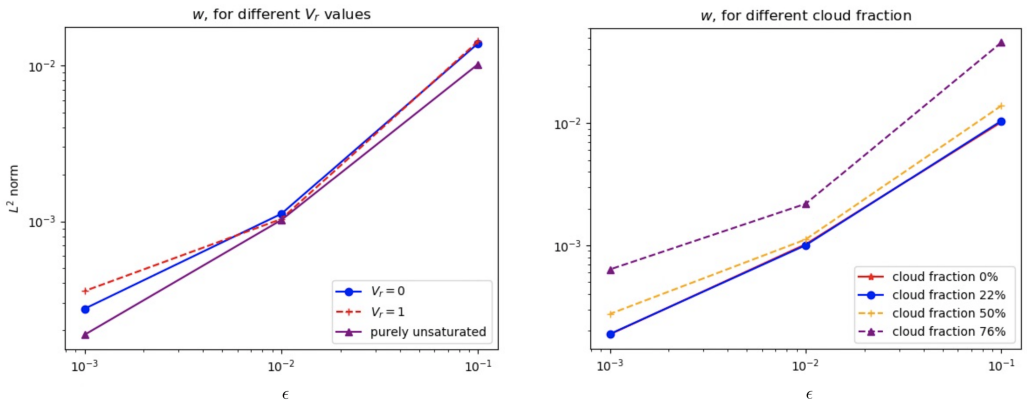

Figure 5. Sensitivity studies for different V_r values (left panel) and cloud fractions (right panel). The plots show the L_2 norm of vertical velocity w vs. the control parameter ϵ. The left panel compares simulations with vapor only (purely unsaturated); both water vapor and liquid water that does not fall ($V_r = 0$); and both water vapor and liquid water that falls at constant speed ($V_r = 1$). For the phase change cases with $V_r = 0$ and $V_r = 1$, the cloud fraction is initially 50%. The right panel varies the initial cloud fraction, allowing for phase changes but no rainfall ($V_r = 0$ fixed). In all cases, the resolution is 128^3 modes and the measurement time is $t = 0.4$.

We also varied the initial cloud fraction while keeping $V_r = 0$ fixed. Considering cloud fractions $0\%, 22\%, 50\%$ and 76%, figure 5 (right) suggests a similar rate of convergence to PQG as ϵ is decreased. However, when cloud fraction is increased, there is an overall higher level of wave activity at $O(1)$ times for fixed ϵ, as indicated by the L^2 norm of vertical velocity. Thus, fast waves appear to be eliminated to a greater degree when the cloud fraction is in the range $0\% - 20\%$, which is typical for cloud fractions in nature.

4. Conclusions

This work considers numerical simulations of a moist Boussinesq system (2.11)-(2.16) with phase changes between water vapor and liquid water, resulting in latent heat release. The focus is on small $Ro = \epsilon \to 0$ and $Fr_1, Fr_2 \sim \epsilon$ in a distinguished limit with one small parameter ϵ, characterizing the flow as strongly rotating, and strongly stably stratified with respect to both equivalent potential temperature and total water. Furthermore, the moist model allows for liquid water to fall as rain.

Starting from random, large-scale, balanced initial conditions in the absence of waves, the numerical simulations with phase changes provide solid evidence that small-amplitude wave activity will be generated on fast $O(\epsilon)$ time scales, but the wave activity does not grow to larger amplitudes, and the system will remain in an almost-balanced state on $O(1)$ time scales. For the run with $\epsilon = 10^{-1}$, cloud fraction 50% and water only in the form of clouds (no rain), wave activity at $t = O(1)$ is 10 times smaller than ϵ and roughly 50 times smaller than the balanced flow components, in the L^2 sense (figure 3). Although there appears to be amplitude-dependence on cloud fraction, the trend is robust, suggesting convergence to the balanced PQG equations in (2.18)–(2.19) and (2.26)-(2.27) as $\epsilon \to 0$ (figure 5 right panel). Finally, the addition of rainfall may also impact both the wave-amplitude and rate of convergence (figure 5 left panel), but does not seem to fundamentally change the trend toward convergence when the fall speed is $O(1)$. These results are similar to what transpires for the dry dynamics, for which rigorous proofs of convergence are found in previous literature [7,8].

The global picture is more complicated when considering unbalanced initial conditions with a significant wave component. In this case, decoupling of fast waves and slowly varying modes has been rigorously proven for the dry dynamics [8,53,59–63], and also holds for purely unsaturated and purely saturated dynamics by a change of variables [18]. On the other hand, previous analytical and numerical work on (2.11)-(2.16) with phase changes suggests that fast-slow coupling persists as $\epsilon \to 0$ [18,19]. Such coupling has been linked to the piecewise nature of waves when phase boundaries are present. In that case, waves change frequency and wavelength across phase interfaces, leading to non-zero averages of the wave-coupling terms on time scales of $O(1)$ [19]. The current work suggest that phase changes and latent heating may not provide additional mechanisms for the generation of waves from balanced or nearly balanced initial conditions.

Note that the present paper provides numerical evidence, but not rigorous proof, of convergence in the $\epsilon \to 0$ limit. The numerical solutions describe not the continuum PDEs but a discrete approximation, characterized by a small grid spacing Δx and small time step Δt. Moreover, the numerical solutions describe not the limiting behavior as $\epsilon \to 0$ but the behavior for small but finite values of ϵ. Under this scenario with multiple types of small parameters $(\Delta x, \Delta t, \epsilon)$, a precise characterization of errors and limits can be challenging. One would perhaps like to take the limit $\Delta x, \Delta t \to 0$ first and then examine the limit $\epsilon \to 0$, or take a distinguished limit where the ratios $\Delta x/\epsilon$ and $\Delta t/\epsilon$ tend to zero as all three parameters tend to zero. In line with these options, the premise here was that the Δx and Δt values were chosen small enough to accurately represent the dynamics on the time scales of interest for the ϵ values under consideration. To test whether the results are robust to changes in Δx and Δt, simulations were carried out with different choices of their values (in terms of number of Fourier modes as 128^3 versus 256^3), and robust results were seen. At the same time, computational expense sets some limitations on Δx and Δt and hence also on the values of ϵ that can be tested. While values as

small as $\epsilon = 10^{-3}$ were tested here, and a trend toward convergence was seen, it is not guaranteed that the trend will continue for smaller, untested values of ϵ.

One future direction is to establish a rigorous proof of convergence (or non-convergence) starting from balanced initial conditions, building upon the intuition gained from the numerical simulations. The proof may require modification from the dry proof using Fourier analysis, which may be complicated by the piece-wise (nonlinear) nature of (2.11)-(2.16) and similar models. From a fundamental physics point of view, it will also be valuable to explore flow structure in this idealized setting with phase changes, but in a wider parameter space, on longer time scales, and with forcing/initial conditions related to atmospheric conditions.

Data Accessibility. Supporting data have been provided as electronic supplementary material along with this article.

Authors' Contributions. Zhang modified Smith's dry code to incorporate phase changes, and performed the numerical simulations. Smith, Stechmann and Zhang analyzed the data and wrote the manuscript.

Competing Interests. The author(s) declare that they have no competing interests.

Funding. This research was partially supported by the US National Science Foundation through grant NSF-DMS-1907667.

Acknowledgements. This article is dedicated to the memory of Charles R. Doering for his leadership, enthusiasm, and lasting contributions to complex systems and nonlinear dynamics. The authors thank Rupert Klein and an anonymous reviewer for helpful comments.

References

1. J. G. Charney, "The dynamics of long waves in a baroclinic westerly current," *J. Meteorol.*, vol. 4, no. 5, pp. 136–162, 1947.
2. J. G. Charney, "On the scale of atmospheric motions," *Geofys. Publ. Oslo*, vol. 17, no. 2, pp. 1–17, 1948.
3. N. A. Phillips, "Energy transformations and meridional circulations associated with simple baroclinic waves in a two-level, quasi-geostrophic model," *Tellus*, vol. 6, no. 3, pp. 273–286, 1954.
4. J. G. Charney, "Geostrophic turbulence," *J. Atmos. Sci.*, vol. 28, no. 6, pp. 1087–1095, 1971.
5. P. B. Rhines, "Geostrophic turbulence," *Ann. Rev. Fluid Mech.*, vol. 11, no. 1, pp. 401–441, 1979.
6. R. Salmon, "Baroclinic instability and geostrophic turbulence," *Geophys. Astro. Fluid*, vol. 15, no. 1, pp. 167–211, 1980.
7. A. J. Bourgeois and J. T. Beale, "Validity of the quasigeostrophic model for large-scale flow in the atmosphere and ocean," *SIAM Journal on Mathematical Analysis*, vol. 25, no. 4, pp. 1023–1068, 1994.
8. A. J. Majda, *Introduction to PDEs and Waves for the Atmosphere and Ocean*, vol. 9 of *Courant Lecture Notes in Mathematics*.
   Providence: American Mathematical Society, 2003.
9. W. W. Grabowski and P. K. Smolarkiewicz, "Monotone finite-difference approximations to the advection-condensation problem," *Monthly Weather Review*, vol. 118, no. 10, pp. 2082–2098, 1990.
10. G. Hernandez-Duenas, A. J. Majda, L. M. Smith, and S. N. Stechmann, "Minimal models for precipitating turbulent convection," *J. Fluid Mech.*, vol. 717, pp. 576–611, 2013.
11. M. Mak, "On moist quasi-geostrophic baroclinic instability," *J. Atmos. Sci.*, vol. 39, pp. 2028–2037, 1982.
12. P. Bannon, "Linear development of quasi-geostrophic baroclinic disturbances with condensational heating," *J. Atmos. Sci.*, vol. 43, pp. 2261–2274, 1986.
13. K. A. Emanuel, M. Fantini, and A. J. Thorpe, "Baroclinic instability in an environment of small stability to slantwise moist convection. Part I: Two-dimensional models," *J. Atmos. Sci.*, vol. 44, no. 12, pp. 1559–1573, 1987.
14. G. Lapeyre and I. M. Held, "The role of moisture in the dynamics and energetics of turbulent baroclinic eddies," *J. Atmos. Sci.*, vol. 61, no. 14, pp. 1693–1710, 2004.
15. H. De Vries, J. Methven, T. Frame, and B. Hoskins, "Baroclinic waves with parameterized effects of moisture interpreted using Rossby wave components," *J. Atmos. Sci.*, vol. 67, pp. 2766–2784, 2010.

16. J. Monteiro and J. Sukhatme, "Quasi-geostrophic dynamics in the presence of moisture gradients," *Q. J. R. Meteorol. Soc.*, vol. 142, pp. 187–195, 2016.
17. L. M. Smith and S. N. Stechmann, "Precipitating quasigeostrophic equations and potential vorticity inversion with phase changes," *J. Atmos. Sci.*, vol. 74, pp. 3285–3303, 2017.
18. Y. Zhang, L. M. Smith, and S. N. Stechmann, "Fast-wave averaging with phase changes: asymptotics and application to moist atmospheric dynamics," *Journal of Nonlinear Science*, vol. 31, no. 38, 2021.
19. Y. Zhang, L. M. Smith, and S. N. Stechmann, "Effects of clouds and phase changes on fast-wave averaging: a numerical assessment," *Journal of Fluid Mechanics*, 2021.
20. R. Klein and A. Majda, "Systematic multiscale models for deep convection on mesoscales," *Theor. Comp. Fluid Dyn.*, vol. 20, pp. 525–551, 2006.
21. A. J. Majda, "Multiscale models with moisture and systematic strategies for superparameterization," *J. Atmos. Sci.*, vol. 64, pp. 2726–2734, 2007.
22. S. N. Stechmann and B. Stevens, "Multiscale models for cumulus cloud dynamics," *J. Atmos. Sci.*, vol. 67, pp. 3269–3285, 2010.
23. B. Khouider, A. J. Majda, and S. N. Stechmann, "Climate science in the tropics: waves, vortices and PDEs," *Nonlinearity*, vol. 26, no. 1, pp. R1–R68, 2013.
24. S. Chen, A. J. Majda, and S. N. Stechmann, "Multiscale asymptotics for the skeleton of the Madden–Julian oscillation and tropical–extratropical interactions," *Math. Clim. Weather Forecast.*, vol. 1, pp. 43–69, 2015.
25. S. Chen, A. J. Majda, and S. N. Stechmann, "Tropical–extratropical interactions with the MJO skeleton and climatological mean flow," *J. Atmos. Sci.*, vol. 73, no. 10, pp. 4101–4116, 2016.
26. S. Hittmeir and R. Klein, "Asymptotics for moist deep convection i: refined scalings and self-sustaining updrafts," *Theoretical and Computational Fluid Dynamics*, vol. 32, no. 2, pp. 137–164, 2018.
27. J. Rosemeier, M. Baumgartner, and P. Spichtinger, "Intercomparison of warm-rain bulk microphysics schemes using asymptotics," *Mathematics of Climate and Weather Forecasting*, vol. 4, no. 1, pp. 104–124, 2018.
28. A. J. Majda and P. E. Souganidis, "Existence and uniqueness of weak solutions for precipitation fronts: A novel hyperbolic free boundary problem in several space variables," *Comm. Pure Appl. Math.*, vol. 63, no. 10, pp. 1351–1361, 2010.
29. M. C. Zelati and R. Temam, "The atmospheric equation of water vapor with saturation," *Bollettino dell'Unione Matematica Italiana*, vol. 5, no. 2, pp. 309–336, 2012.
30. M. C. Zelati, M. Frémond, R. Temam, and J. Tribbia, "The equations of the atmosphere with humidity and saturation: uniqueness and physical bounds," *Physica D: Nonlinear Phenomena*, vol. 264, pp. 49–65, 2013.
31. A. Bousquet, M. C. Zelati, and R. Temam, "Phase transition models in atmospheric dynamics," *Milan Journal of Mathematics*, vol. 82, no. 1, pp. 99–128, 2014.
32. M. C. Zelati, A. Huang, I. Kukavica, R. Temam, and M. Ziane, "The primitive equations of the atmosphere in presence of vapour saturation," *Nonlinearity*, vol. 28, no. 3, p. 625, 2015.
33. J. Li and E. S. Titi, "A tropical atmosphere model with moisture: global well-posedness and relaxation limit," *Nonlinearity*, vol. 29, no. 9, p. 2674, 2016.
34. S. Hittmeir, R. Klein, J. Li, and E. S. Titi, "Global well-posedness for passively transported nonlinear moisture dynamics with phase changes," *Nonlinearity*, vol. 30, no. 10, p. 3676, 2017.
35. Y. Cao, M. Hamouda, R. Temam, J. Tribbia, and X. Wang, "The equations of the multi-phase humid atmosphere expressed as a quasi variational inequality," *Nonlinearity*, vol. 31, no. 10, p. 4692, 2018.
36. S. Hittmeir, R. Klein, J. Li, and E. S. Titi, "Global well-posedness for the primitive equations coupled to nonlinear moisture dynamics with phase changes," *Nonlinearity*, vol. 33, pp. 3206–3236, 2020.
37. A. N. Wetzel, L. M. Smith, and S. N. Stechmann, "Moisture transport due to baroclinic waves: Linear analysis of precipitating quasi-geostrophic dynamics," *Math. Clim. Weather Forecast.*, vol. 3, no. 1, pp. 28–50, 2017.
38. A. N. Wetzel, L. M. Smith, and S. N. Stechmann, "Discontinuous fronts as exact solutions to precipitating quasi-geostrophic equations," *SIAM J. Appl. Math.*, vol. 79, pp. 1341–1366, 2019.
39. A. N. Wetzel, L. M. Smith, S. N. Stechmann, and J. E. Martin, "Balanced and unbalanced components of moist atmospheric flows with phase changes," *Chin. Ann. Math. Ser. B*, vol. 40, pp. 1005–1038, 2019.

40. A. N. Wetzel, L. M. Smith, S. N. Stechmann, J. E. Martin, and Y. Zhang, "Potential vorticity and balanced and unbalanced moisture," *J. Atmos. Sci.*, vol. 77, pp. 1913–1931, 2020.
41. D. H. Marsico, L. M. Smith, and S. N. Stechmann, "Energy decompositions for moist Boussinesq and anelastic equations with phase changes," *Journal of the Atmospheric Sciences*, vol. 76, pp. 3569–3587, 2019.
42. T. K. Edwards, L. M. Smith, and S. N. Stechmann, "Atmospheric rivers and water fluxes in precipitating quasi-geostrophic turbulence," *Quarterly Journal of the Royal Meteorological Society*, vol. 146, pp. 1960–1975, 2020.
43. T. K. Edwards, L. M. Smith, and S. N. Stechmann, "Spectra of atmospheric water in precipitating quasi-geostrophic turbulence," *Geophysical & Astrophysical Fluid Dynamics*, p. in press, 2020.
44. R. Hu, T. K. Edwards, L. M. Smith, and S. N. Stechmann, "Initial investigations of precipitating quasi-geostrophic turbulence with phase changes," *Research in the Mathematical Sciences*, vol. 8, no. 6, 2021.
45. H. L. Kuo, "Convection in conditionally unstable atmosphere," *Tellus*, vol. 13, no. 4, pp. 441–459, 1961.
46. G. Sommeria, "Three-dimensional simulation of turbulent processes in an undisturbed trade wind boundary layer," *J. Atmos. Sci.*, vol. 33, no. 2, pp. 216–241, 1976.
47. C. S. Bretherton, "A theory for nonprecipitating moist convection between two parallel plates. Part I: Thermodynamics and "linear" solutions," *J. Atmos. Sci.*, vol. 44, pp. 1809–1827, 1987.
48. J. W. M. Cuijpers and P. G. Duynkerke, "Large eddy simulation of trade wind cumulus clouds," *J. Atmos. Sci.*, vol. 50, no. 23, pp. 3894–3908, 1993.
49. S. N. Stechmann, "Multiscale eddy simulation for moist atmospheric convection: Preliminary investigation," *J. Comput. Phys.*, vol. 271, pp. 99–117, 2014.
50. K. Spyksma, P. Bartello, and M. K. Yau, "A Boussinesq moist turbulence model," *J. Turbulence*, vol. 7, no. 32, pp. 1–24, 2006.
51. O. Pauluis and J. Schumacher, "Idealized moist Rayleigh–Bénard convection with piecewise linear equation of state," *Commun. Math. Sci*, vol. 8, pp. 295–319, 2010.
52. G. Hernandez-Duenas, L. M. Smith, and S. N. Stechmann, "Stability and instability criteria for idealized precipitating hydrodynamics," *J. Atmos. Sci.*, vol. 72, no. 6, pp. 2379–2393, 2015.
53. A. Babin, A. Mahalov, B. Nicolaenko, and Y. Zhou, "On the asymptotic regimes and the strongly stratified limit of rotating boussinesq equations," *Theoretical and computational fluid dynamics*, vol. 9, no. 3-4, pp. 223–251, 1997.
54. C. Snyder, D. J. Muraki, R. Plougonven, and F. Zhang, "Inertia-gravity waves generated within a dipole vortex," *J. Atmos. Sci.*, vol. 64, pp. 4417–4431, 2007.
55. C. Snyder, R. Plougonven, and D. J. Muraki, "Mechanisms for spontaneous gravity wave generation within a dipole vortex," *J. Atmos. Sci.*, vol. 66, pp. 3464–3487, 2009.
56. J. Vanneste and I. Yavneh, "Exponentially small inertia-gravity waves and the breakdown of quasigeostrophic balance," *J. Atmos. Sci.*, vol. 61, p. 211–223, 2004.
57. J. Vanneste, "Balance and spontaneous wave generation in geophysical flows," *Annu. Rev. Fluid Mech.*, vol. 45, pp. 147–172, 2013.
58. G. Hernandez-Duenas, L. M. Smith, and S. N. Stechmann, "Investigation of Boussinesq dynamics using intermediate models based on wave–vortical interactions," *J. Fluid Mech.*, vol. 747, pp. 247–287, 2014.
59. P. F. Embid and A. J. Majda, "Averaging over fast gravity waves for geophysical flows with arbitary potential vorticity," *Comm. PDEs*, vol. 21, no. 3-4, pp. 619–658, 1996.
60. P. F. Embid and A. J. Majda, "Low Froude number limiting dynamics for stably stratified flow with small or finite Rossby numbers," *Geophys. Astrophys. Fluid Dynam.*, vol. 87, no. 1-2, pp. 1–50, 1998.
61. A. J. Majda and P. Embid, "Averaging over fast gravity waves for geophysical flows with unbalanced initial data," *Theor. Comput. Fluid Dyn.*, vol. 11, no. 3-4, pp. 155–169, 1998.
62. A. Babin, A. Mahalov, and B. Nicolaenko, "Fast singular oscillating limits and global regularity for the 3d primitive equations of geophysics," *ESAIM: Mathematical Modelling and Numerical Analysis*, vol. 34, no. 2, pp. 201–222, 2000.
63. A. Babin, A. Mahalov, and B. Nicolaenko, "Global splitting, integrability and regularity of 3d euler and navier-stokes equations for uniformly rotating fluids," *European Journal of Mechanics, B/Fluids*, vol. 15, no. 3, pp. 291–300, 1996.